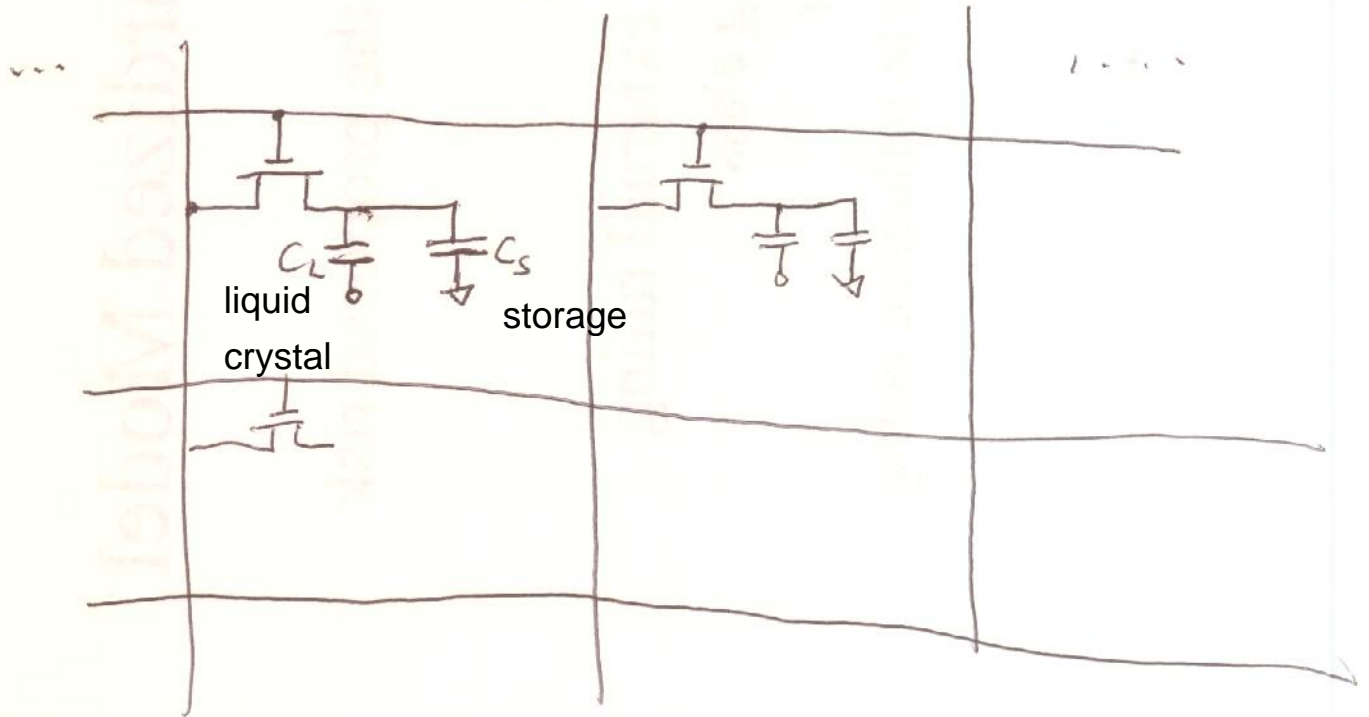


# Thin film Transistors (TFTs)

Materials:

material	mobility ( $\text{cm}^2/\text{Vs}$ )
$\alpha\text{-Si:H}$ (n only)	0.6 - 1
poly-Si, n	50 - 400
poly-Si, p	15 - 70
organics, p (n-channel materials are being developed)	$10^{-3}$ - 10

Why are these lousy materials needed?



Amorphous Si = a-Si:H

- Tetrahedral bonding in Si
- Due to  $sp^3$  hybridization.
- Local order (tetrahedral) largely unchanged (long range disorder)
- Band structure similar to c-Si

Bonding  $\Leftrightarrow$  Valence band

Anti bonding  $\Leftrightarrow$  Conduction band.

- But, due to lack of long range order (periodicity), there's no such thing as  $k$ !
  - No Bloch theorem.
  - No translational symmetry.

# Amorphous Silicon Electronics

R.A. Street

## Introduction

The progressive miniaturization of electronics is familiar to everyone; computing power that used to occupy a room can now be put onto a single integrated circuit. Miniaturization is admirable when size is not relevant to the electronic function, but there are plenty of devices in which a large physical size is essential. Many of these concern information technology, examples being the computer display, printer, and fax machine. Communication with the electronic world is primarily visual and operates at a large format typified by a document. In this rapidly advancing field, we are eagerly awaiting desktop interactive display surfaces that can input as well as display information, document readers, truly portable computers, electronic vision and—the oldest dream of all—the television that hangs on the wall. Realization of these hopes requires a set of technologies that permit bigger rather than smaller electronic systems, and amorphous silicon is helping to make this happen.

Crystalline silicon does not cope well with the large sizes needed for electronics at the human interface. Of the many technologies used in present devices, the CRT is the oldest and most successful for displays, printers use moving heads or spinning mirrors, and many other devices use optical projection. Large-area electronic devices add a new dimension to this crowded field. These use circuits similar to those in crystalline silicon but made by the square foot rather than the square inch. Such devices are based on thin-film semiconductors deposited on a convenient substrate, avoiding the necessity of growing large single crystals.

Hydrogenated amorphous silicon (a-Si:H) has existed in its present form for about 20 years,<sup>1</sup> and has made the transition from experimental curiosity to standard material, with broad applications in solar cells, displays, printers, and imaging devices.

The first commercial amorphous silicon devices were photovoltaic solar cells, which in 1980 were introduced by Sanyo into consumer products such as handheld calculators. As the efficiency of devices increases, and manufacturing costs decrease, the goal of employing photovoltaic power on a large scale becomes more achievable. Today, amorphous silicon is being used as a photoreceptor in copiers, utilizing the ability to deposit the material

a-Si:H

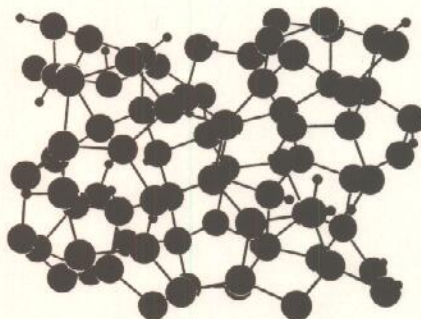


Figure 1. Model of the atomic structure of a-Si:H illustrating the bonding disorder and the presence of hydrogen. Large disks represent silicon atoms and small disks are hydrogen.

*mobility gap 1.85 eV*  
*E<sub>g</sub> = 1.1 eV for single crystalline Si.*

over large areas. The most exciting and rapidly growing technological developments in this area, however—and the focus of this paper—are the matrix-addressed arrays. These are multiple pixel devices used for imaging and display. Amorphous silicon optical scanners were first introduced into fax machines in the mid-1980s and now comprise about half the market. Mass production of liquid crystal displays driven by amorphous silicon transistors began in 1987, and their development is particularly rapid now. The prospects for large-area detector devices, including medical x-ray imaging, appear attractive.

The application of amorphous semiconductors to large-area electronics is not new. Selenium photoreceptors enabled the first Xerox copier machines 35 years ago. What is new is the extra functionality provided by the matrix-addressed silicon arrays, which permits electronic reprographics and display in a way not possible with the simple photoreceptor.

## Amorphous Silicon

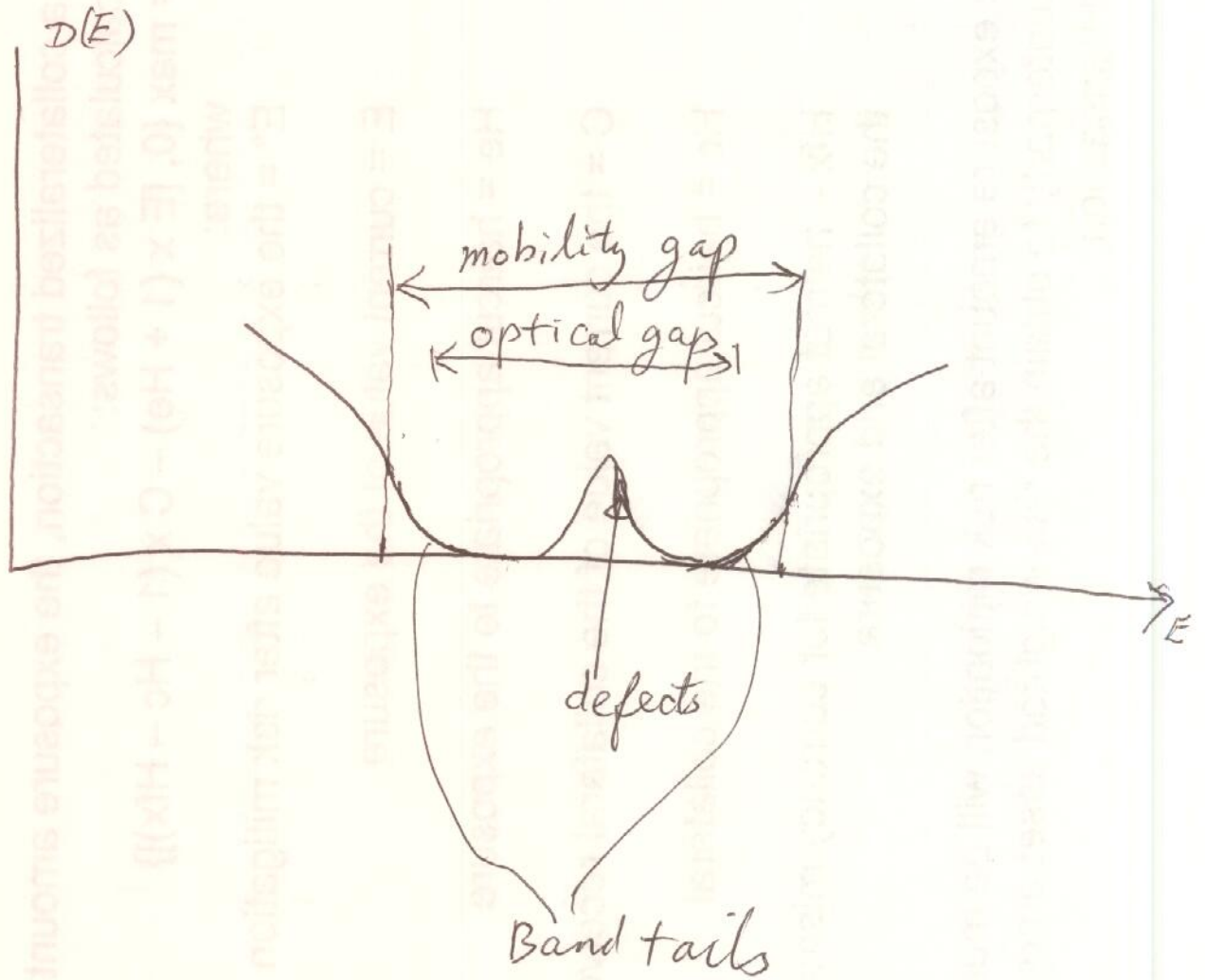
Amorphous silicon is deposited from silane gas (SiH<sub>4</sub>) by plasma-enhanced chemical vapor deposition. The plasma provides the energy to dissociate the silane which initiates film growth, although the complex chemical process of deposition is still not completely understood. Films are usually grown at 200–300°C, and virtually any material that can stand this temperature is a suitable substrate, although glass is the most common. The reactor can be scaled to large size, and deposition systems with substrates measuring many square feet presently produce solar cells.

Amorphous silicon has standard semiconducting properties. It has an optical bandgap of about 1.7 eV, exhibits n-type and p-type doping by the addition of phosphorus- or boron-containing gases to the deposition reactor, and is highly photoconductive.<sup>3</sup> The material owes most of its useful properties (but also some problems) to the presence of about 10 at.% of hydrogen, which originates from the SiH<sub>4</sub> deposition gas. The hydrogen reduces the

Table I: Some Typical Room-Temperature Electrical Properties of Hydrogenated Amorphous Silicon, as Compared to Crystalline Silicon.

	a-Si:H	Crystalline Si
Electron mobility	1 cm <sup>2</sup> /Vsec	1300 cm <sup>2</sup> /Vsec
Hole mobility	3 × 10 <sup>-3</sup> cm <sup>2</sup> /Vsec	500 cm <sup>2</sup> /Vsec
n-type conductivity	10 <sup>-2</sup> Ω <sup>-1</sup> cm <sup>-1</sup>	10 <sup>2</sup> Ω <sup>-1</sup> cm <sup>-1</sup>
p-type conductivity	10 <sup>-4</sup> Ω <sup>-1</sup> cm <sup>-1</sup>	10 <sup>2</sup> Ω <sup>-1</sup> cm <sup>-1</sup>

Density of States  $D(E)$  is still a valid concept.



Extended states & localized states

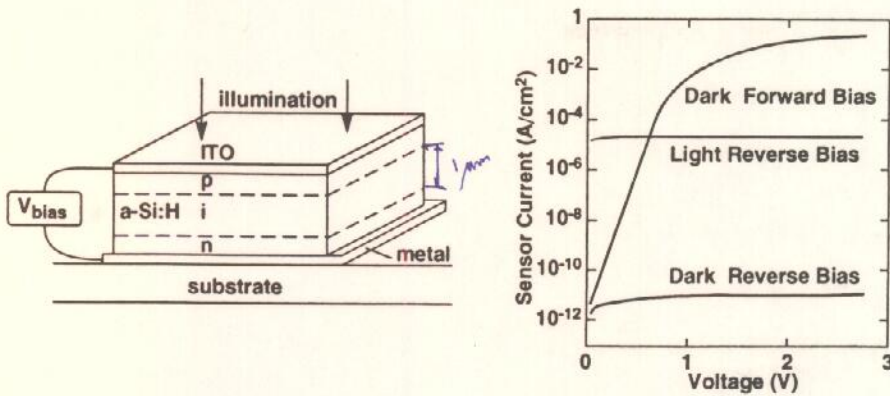


Figure 2. Structure of the n-i-p sensor and its electrical characteristics in forward and reverse bias.

of the design are tailored to the material properties. The usual sensor structure, shown in Figure 2, is an n-i-p device in which the undoped i-layer is about 1  $\mu\text{m}$  thick and the doped n- and p-layers are about 10 nm. The high-defect density of doped a-Si:H makes it insensitive to light, as compared with the undoped layer. The doped layers are therefore present only to provide an electrical junction with low reverse bias leakage current, and are made as thin as possible to avoid optical absorption losses. Fortunately, the same high-defect density gives them a small depletion layer width, and a 10-nm film is sufficient.

The low carrier mobility of a-Si:H suppresses diffusion currents in the undoped layer and efficient charge collection requires an internal electric field. Undoped a-Si:H has a depletion width of about 1  $\mu\text{m}$  at zero bias, placing an upper limit on the thickness of solar cells. A reverse bias extends the depletion layer, even up to 50–100  $\mu\text{m}$ , but present array processing technology limits the thickness to 1–3  $\mu\text{m}$ , and such sensors exhibit full collection at a modest reverse bias (see Figure 2). The atomic disorder of a-Si:H eliminates the indirect bandgap of crystalline silicon, so that a 1- $\mu\text{m}$ -thick film absorbs light across the whole visible spectrum, with its peak quantum efficiency reaching 90–95%, and conveniently centered at 500–600 nm.

The thin sensor has a capacitor structure and therefore provides its own storage of the light-induced charge. A sensor measuring 100 $\times$ 100  $\mu\text{m}$  has a capacitance of about 1 pF and its charge storage capacity is equivalent to the charge generated by room-light exposure for about 0.1 msec.

The thin-film field effect transistor (TFT) is similarly designed around the specific electronic properties of a-Si:H. The undoped channel avoids the high defect density of doped material, and the TFT is operated under electron accumulation because the electron mobility is much higher than that of holes (see Table I). The usual gate dielectric is silicon nitride, which has the advantage of being deposited in the same reactor as a-Si:H by addition of  $\text{NH}_3$  to the gas mixture. One of the common TFT structures is shown in Figure 3. The gate is deposited first, partly because the optimum growth temperature of the nitride is higher than of a-Si:H, and partly because a better interface results when the nitride is deposited first, for reasons that are poorly understood. The thin active layer of the TFT is typically about 50 nm, and the source-drain contacts are n-type a-Si:H, to give good electron injection and to block holes. A top nitride passivation layer prevents leakage along the top interface.

The electronic characteristics of the TFT

density of electronic defects formed by silicon dangling bonds to about  $10^{15} \text{ cm}^{-3}$ . The atomic structure in Figure 1 illustrates the disorder and the hydrogen bonding.

Devices made from a-Si:H are designed around the specific material properties, particularly of the doped films. Although a high concentration of impurity dopant atoms can be introduced into a-Si:H, the effectiveness of doping is low. The doped material has a higher defect density than undoped a-Si:H, reaching above  $10^{18} \text{ cm}^{-3}$  for 1 at.% dopant incorporation and these act as compensation centers. In addition, not all the impurity atoms are active dopants, and the fraction decreases at increased concentrations. The conductivity of doped a-Si:H is further reduced by the low carrier mobility, which is a consequence of both the frequent scattering by the atomic disorder and the presence of localized trapping states near the band edge. Table I compares the electronic properties of amorphous and crystalline silicon. Although the electronic properties are clearly much poorer in the amorphous state than in the crystal, they are sufficient for the needs of most matrix-addressed arrays.

Like most materials, a-Si:H has its problems. A particular concern for many device applications is its inherent structural instability, first observed as a light-induced increase in defect density that caused solar cells to degrade slowly during operation. This effect is caused by the migration of hydrogen, which creates dangling bond defects as it detaches from a Si-H bond. The instability is induced by the presence of nonequilibrium carriers and is therefore a potential problem in any electronic device. Fortunately, the effect occurs very slowly at room temperature and hardly interferes with the matrix-addressed arrays, although it limits their operation to

below 50°C. Much of this materials research effort is aimed at mitigating the instability problem.

Sensors and Transistors

Optical sensors and field effect transistors are the two important active devices used in the array technology. Both have structures generically similar to their crystalline counterparts, although the details

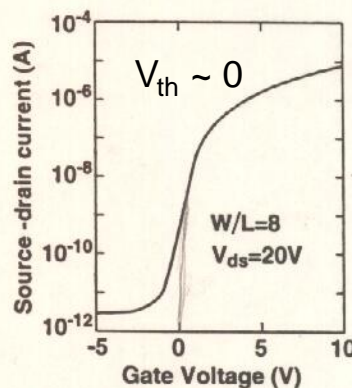
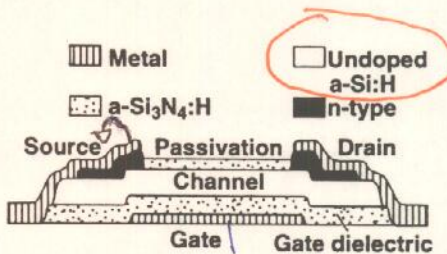


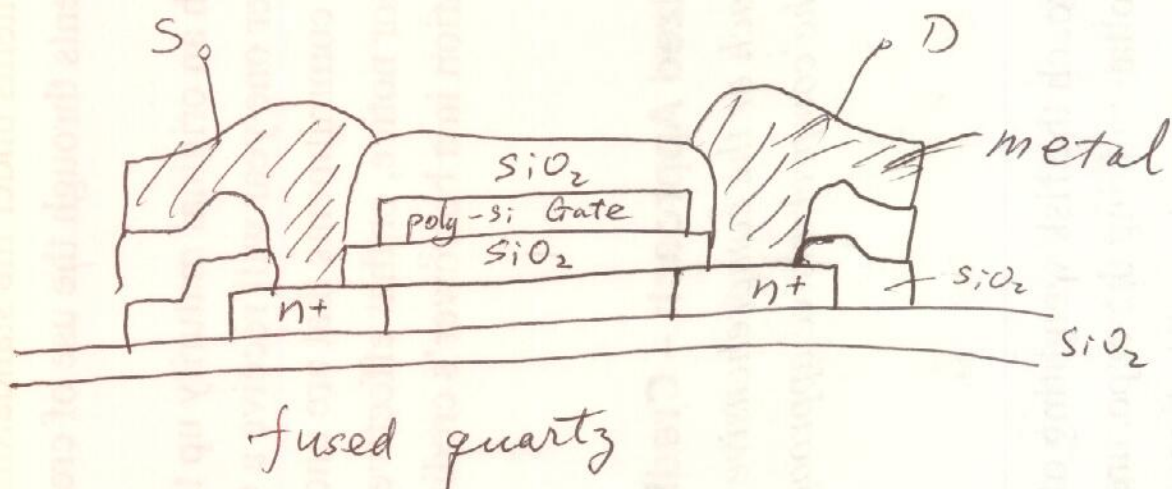
Figure 3. Structure of the field effect thin-film transistor (TFT) and its typical electrical transfer characteristics for a source-drain voltage of 20 V.

Electron accumulation mode

# Polycrystalline Si - poly-Si

Higher mobility, both n- & p-channel devices available; higher temperature, higher cost.

Polycrystals, domains (grains), boundaries.



## Fabrication:

$\text{SiO}_2$  buffer layer: LPCVD/PECVD, 400°C; 500 nm

poly-Si channel precursor: " 350-550°C, 50-100 nm

" crystallization: Furnace 500-600°C,  
RTA, or laser.

poly-Si island etch

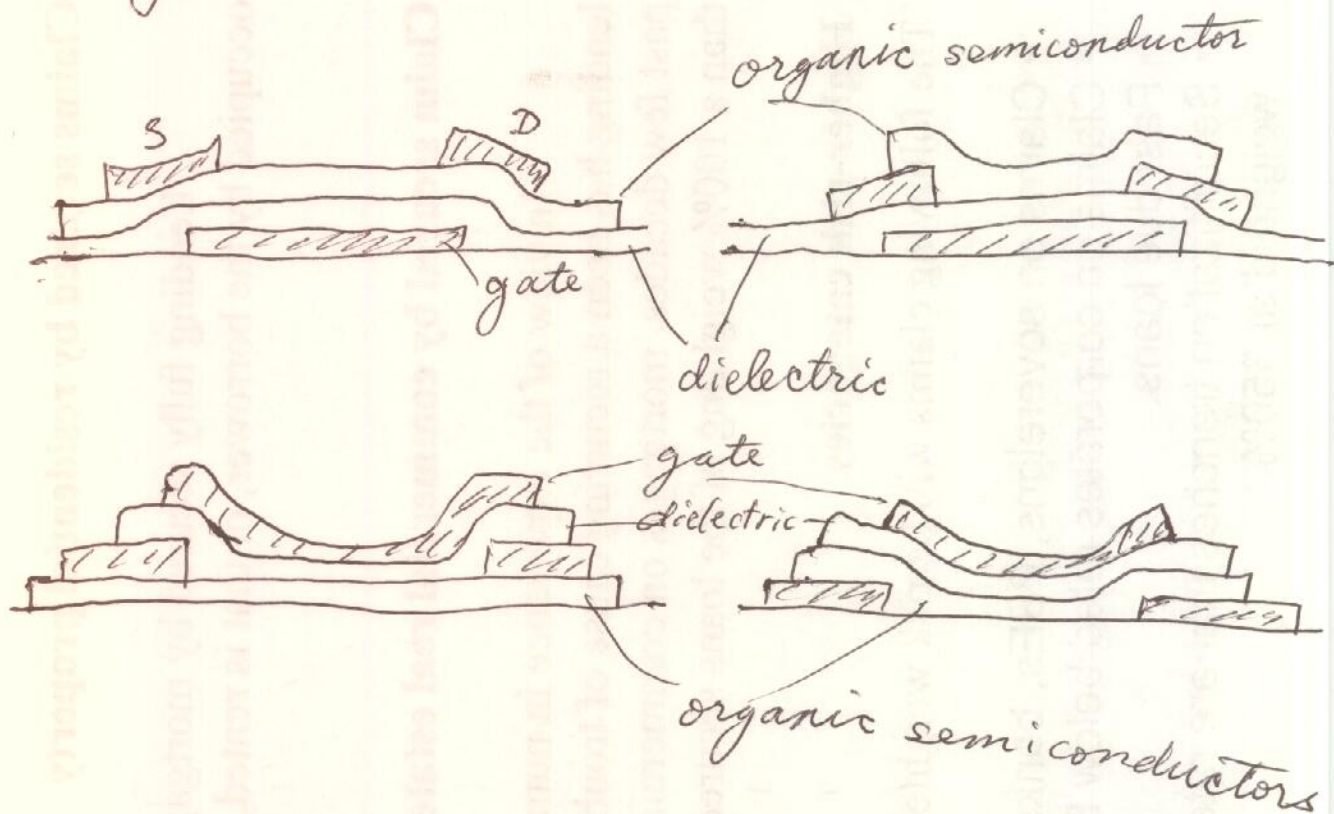
Gate dielectric deposition: LPCVD/PECVD

Gate dielectric anneal: 600°C

Poly-Si gate deposition: LPCVD/PECVD 350-550°C

" Etch

# Organic TFTs (OTFTs)



- Most organic semiconductors are sensitive to solvents - can't use photolithography.
- But patterning is needed. Often done w/ shadow masks during deposition
- Choice of device configuration often dictated by this limitation in patterning.
- S/D contacts formed by metals (No doping, no self-alignment)  
Choice of contact metal

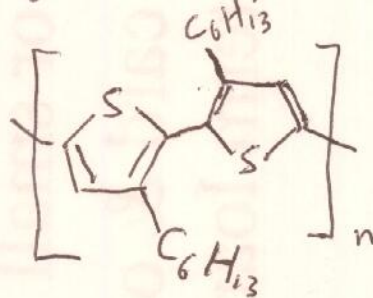
Organic semiconductor channel materials.

Polycrystalline molecular thin films

small molecule example: pentacene

polymer example:

poly(3-hexylthiophene), P3HT



# Organic Molecules – Electronic Structures, Properties, and Reactions

## 1 Introduction

Several chapters of this book describe the utilization of organic molecules for novel electronic devices: Carbon Nanotubes for Data Processing (Chap. 19), Molecular Electronics (Chap. 20), Neurobiological Interface (Chap. 32), Liquid Crystal Displays (Chap. 37), and Organic LEDs (Chap. 38). For this reason, here we give a very brief introduction to organic chemistry, focusing on the requirements of the devices chapters.

Section 2 summarizes the main classes of hydrocarbons and bond types, then Sec. 3 applies the methods of quantum mechanics (Chap. 3) to hydrocarbons. Finally, Sec. 4 introduces the functional groups and the major types of reaction mechanisms. Because space is limited, the reader should refer to the standard textbooks on organic chemistry and physical chemistry, for example, Refs. [1] – [6], in order to obtain a deeper understanding of the subject.

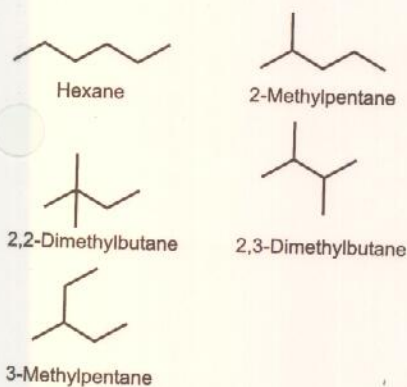


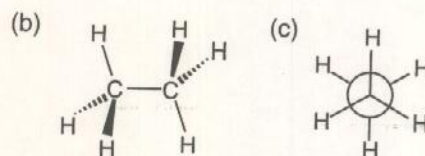
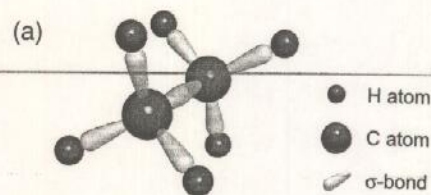
**Figure 2:** Structural isomers of hexane  $C_6H_{14}$ . According to the rules of the IUPAC (International Union of Pure and Applied Chemistry), the names of the isomers are based on the longest continuous carbon chain as the root, with branching groups named as substituents. The position in the root to which an alkyl group is attached is designated by number, starting at the end closest to the attachment. For this figure, the line notation of the organic chemistry is used. This notation represents the presence of C-H C-C bonds by single lines. The presence of C-H bonds is inferred as needed to meet the valence requirements of carbon.

3 valence e's each in  $sp^2$   
1 in  $p_z$

## 2 Hydrocarbons

Saturated hydrocarbons are called **alkanes** and have molecular formula  $C_nH_{2n+2}$ . The chemical bonding in alkanes can be described as  $sp^3$  hybridization of the atomic orbitals (AO) at the carbon atoms, corresponding to a tetrahedral arrangement of the  $\sigma$ -bonds with the neighboring C and H atoms. As an example, Figure 1 shows the configuration of ethane,  $C_2H_6$ . Free rotation is possible around the C—C  $\sigma$ -bond with an activation energy of about 0.1 eV. For alkanes with  $n > 3$ , there are structural **isomers** (different arrangements of the same numbers of atoms) in the form of chains and branched molecules, as illustrated in Figure 2 for hexane,  $C_6H_{14}$ . Alkanes with a ring-type structure are called **cycloalkanes**. Figure 3 shows the structure of cyclohexane, for example.

Hydrocarbons with C=C double bonds are called **alkenes**. The  $sp^2$  hybridization of the carbon AOs corresponds to a trigonal planar configuration of the  $\sigma$ -bonds with the neighboring C and H atoms. The remaining p-AOs at neighboring C atoms take part in bonding, for which the electron density is not concentrated along the axis connecting the two bonded atoms as in the  $\sigma$ -bonds, but is located above and below the axis (Figure 4) with its plane of maximum electron density normal to the plane of  $\sigma$ -bonds. The length of a C=C double bond is 134 pm whereas that of a C-C single bond is



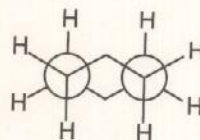
$sp^3$

**Figure 1:** Representations of ethane,  $C_2H_6$ .  
(a) Structural representation of the bonds.  
(b) Sawhorse presentation.  
(c) Stereo projection along the C-C axis.

4 valence electrons each C,  
all in  $sp^3$



**Figure 3:** Structural representation of cyclohexane,  $C_6H_{12}$ .



$sp^2$

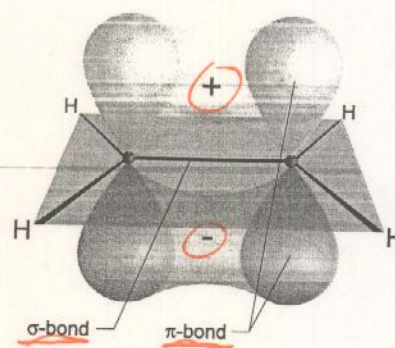


**Figure 4:** Illustration of the  $\pi$ -bond of ethene,  $C_2H_4$ , resulting from the co-planar p-AOs of the  $sp^2$  hybridized C atoms. For clarity of the picture, the  $\sigma$ -bonds are not shown in their full shape.

signs of the wavefunction  
not charge

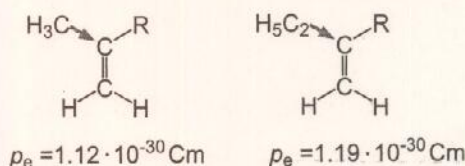


Figure 5: Dipole moment for alkenes in which the double bond is located asymmetrically within the molecule.

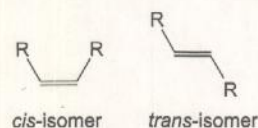


Figure 6: *Cis*- and *trans*-isomers of an alkene molecule. R indicates an alkyl substituent.

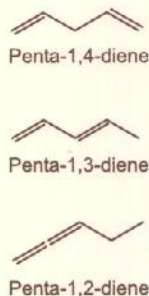


Figure 7: Types of polyenes illustrated by different penta-dienes. Penta-1,4-diene shows isolated double bonds, penta-1,3-diene shows conjugated double bonds, and penta-1,2-diene shows cumulated double bonds. Since the C atom in the center of the cumulated double bond is  $sp$ -hybridized, this double bond is linear.

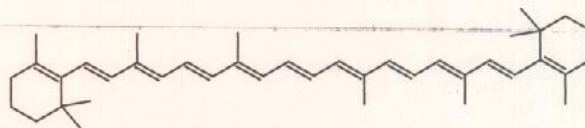


Figure 8:  $\beta$ -Carotene as an example for a polyene with long conjugated double bonding system.

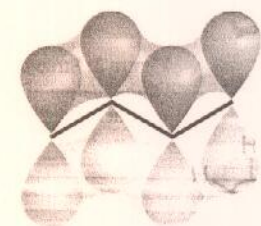
$\sigma$ -bonds form the skeleton of the molecule.  
 $\pi$ -bonds are electronically active.

154 pm. In contrast to single bonds, free rotation is not possible for double bonds since this would require the breaking of the  $\pi$ -bond. The physical properties of alkenes, such as melting and boiling temperatures and solubilities in various solvents, are similar to those of the alkanes. However, whereas alkanes are virtually non-polar, i.e. they have zero permanent electric dipole moment,  $p_e$ , asymmetric alkenes are slightly polar. This indicates that alkyl groups exhibit a weak electron donating effect ( $+I$  effect, see below), as illustrated in Figure 5. When different groups are attached on each side of a double bond, we distinguish between *cis*- and *trans*-isomers (Figure 6).

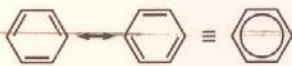
If there are more than one  $C=C$  bond in a molecule, the compounds are called **polyenes**. Depending on the different relative positions of the  $C=C$  bonds, the bonds are referred to as isolated, conjugated, and cumulated as shown in the example of pentadiene in Figure 7. As will be discussed later, conjugated  $C=C$  bonds play an important role in electron conduction because  $\pi$ -electrons are delocalized over the entire extent of conjugation.  $\beta$ -Carotene is an example of a naturally occurring polyene (Figure 8), and contributes to the colour of vegetation.

Cyclic polyenes with conjugation that spreads over an entire ring of atoms sequence constitute the class of **aromatic hydrocarbons**, or **arenes**. If they are planar (which permits overlap of adjacent p-AOs) and possess  $4n+2$  electrons with  $n = 1, 2, \dots$  in the  $\pi$ -system (the Hückel criterion of aromaticity), they exhibit a high energetic stability. The  $\pi$ -electrons are delocalized over the entire ring and single and double bonds can no longer be distinguished: one consequence is the identity of bond lengths round the ring. The most prominent and important representative is cyclohexa-1,3,5-triene, which is universally called benzene (Figure 9). The electronic structure and the origin of the stability of aromatic rings with six  $\pi$ -electrons (i.e.  $n = 1$  for the Hückel criterion) as in benzene will be discussed in Sec. 3.2. The pronounced stability and the delocalization of the  $\pi$ -electrons is maintained for fused rings, the so-called **polycyclic aromatic molecules**, (Figure 10), and for smaller or larger rings provided the number of  $\pi$ -electrons is kept at six (an electron sextet). As examples of the latter, Figure 11 shows a cyclopentadienyl anion and a cycloheptatrienyl cation. In addition, azulene can be regarded as a fused-ring of a cycloheptatriene and a cyclopentadiene. The Hückel stability criterion based on electron sextets can be extended to heterosubstituents in the carbon ring as shown in Figure 12 for some common hexagonal and pentagonal ring systems.

Hydrocarbons with  $C\equiv C$  triple bonds are called **alkynes**. The C atoms participating in the triple bond are  $sp$ -hybridized and the bond consists of one  $\sigma$ -bond and two  $\pi$ -bonds. The  $\sigma$ -bond connecting triply bonded C atoms is surrounded by a cylindrical cloud of  $\pi$ -electron density (Figure 13). The bond length is 120 pm, which is shorter than for single and double bonds. Because of the linearity of a triple bond with its adjacent single bonds, no *cis/trans* isomerism exists. Conjugated triple bonds show the same electron delocalization as conjugated double bonds. Because of this delocalization and their simple linear structure they are sometimes regarded as rigid rods and are of great interest for molecular electronic systems.



$sp^2$



For entire ring, 6  $p_z$  electrons.

Figure 9: Structure and illustration of the electron density of the  $\pi$ -conjugated system of benzene. The two mesomeric Kekulé formulas according to the valence-bond theory as well as the frequently used Robinson ring symbol are shown.

## Pentacene ultrathin film formation on reduced and oxidized Si surfaces

Ricardo Ruiz,<sup>1</sup> Bert Nickel,<sup>2,3</sup> Norbert Koch,<sup>3,4</sup> Leonard C. Feldman,<sup>1</sup> Richard F. Haglund,<sup>1</sup> Antoine Kahn,<sup>3,4</sup> and Giacinto Scoles<sup>2,3</sup><sup>1</sup>Vanderbilt University, Department of Physics and Astronomy, Nashville, Tennessee, 37235<sup>2</sup>Princeton University, Chemistry Department, Princeton, New Jersey, 08544<sup>3</sup>Princeton Materials Institute, Princeton, New Jersey, 08544<sup>4</sup>Princeton University, Department of Electrical Engineering, Princeton, New Jersey, 08544

(Received 3 September 2002; published 12 March 2003)

We have compared the nucleation of pentacene on reduced and oxidized Si surfaces by a combination of x-ray reflectivity measurements and atomic force microscopy. For the reduced surface, the nucleation density is  $0.007 \mu\text{m}^{-2}$ . Second monolayer (ML) formation starts at a coverage of  $\Theta=0.6$  ML, and the first layer is completely closed at a total coverage of 2 ML. For the oxidized surface, the nucleation density is larger by a factor of 100 ( $0.7 \mu\text{m}^{-2}$ ). Second ML formation also starts at  $\Theta=0.6$  ML, but the first layer closes already at 1.1 ML coverage, indicating nearly ideal layer-by-layer growth. For both terminations, the electron density obtained for the closed first monolayer is only 75% of the bulk value, indicating a reduced mass packing efficiency of the layer. Second ML islands are aligned relative to each other on an area limited by the lateral size of first ML islands, which act as templates for epitaxial growth.

DOI: 10.1103/PhysRevB.67.125406

PACS number(s): 68.55.Ac, 61.10.Kw, 61.66.Hq

## I. INTRODUCTION

Organic/inorganic interfaces are currently under investigation due to their critical role in molecular and bioelectronic technology.<sup>1-3</sup> Among the various materials being studied, pentacene ( $\text{C}_{22}\text{H}_{14}$ ), a long, flat, aromatic molecule (see Fig. 1) is particularly promising for electronic applications. Pentacene forms good crystals if deposited onto flat, inert surfaces, resulting in highly anisotropic transport properties.<sup>4</sup> Pentacene is used to fabricate organic thin film transistors (OTFT's) in applications where large area coverage, mechanical flexibility, and room temperature processing are required.<sup>5,6</sup> In such devices, high field-effect mobilities up to  $1.5 \text{ cm}^2/(\text{Vs})$ <sup>7</sup> have been reported along with a variety of OTFT configurations and designs.<sup>3,8,9</sup>

Charge transport in an OTFT is confined to the first few monolayers in close proximity to the gate oxide (the channel).<sup>10</sup> Extensive work has been devoted to determine and optimize the charge transport properties of mesoscopic pentacene films (thickness range from 10 nm to  $1 \mu\text{m}$ )<sup>11-14</sup> and to relate these properties to the crystalline structure and morphology. However, in order to disentangle structural aspects from fundamental limits of charge transport in organic materials, the confinement of the charge transport towards the gate oxide demands a detailed study of the early stages of film formation since these layers dominate charge transport.

In this paper we report a combined atomic force microscopy (AFM) and synchrotron x-ray reflectivity differential study of pentacene film formation on two different surface terminations [Fig. 1(e,f)] prepared by applying standard wet etching techniques to a thermally oxidized Si wafer. In our analysis, we focus on the coverage and structure of the first few monolayers. Our work is complementary to recent experiments, in which photoelectron emission microscopy (PEEM) demonstrated that pentacene film formation can be improved considerably by making use of a cyclohexane termination of clean Si(001) surfaces<sup>15</sup> or by means of hyper-

thermal beam-deposition energies.<sup>16</sup> Here, we demonstrate that similar full first layer coverage and layer-by-layer growth may also be achieved for clean oxide and H-terminated Si surfaces. We also demonstrate that different substrate terminations, having dissimilar surface energies, result in completely different morphologies and nucleation densities.

## II. EXPERIMENTAL DETAILS

## A. Substrate preparation

Since pentacene film formation is controlled by relatively weak van der Waals interactions, nucleation of the first monolayer (ML) is extremely sensitive to defects or impurities on the substrate surface which act as pinning centers. Heterogeneous surfaces lead to a wide range of morphologies and piling up of material, making the interpretation of properties, such as field effect mobility, difficult. To minimize the influence of surface impurities, we have applied the

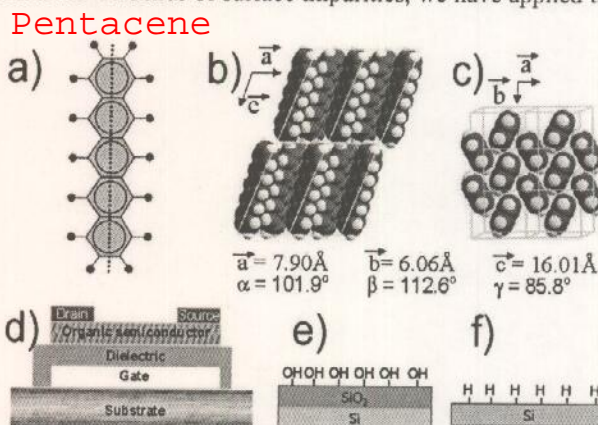
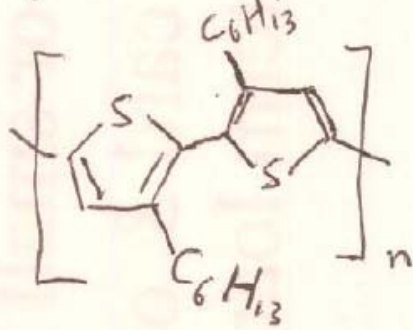


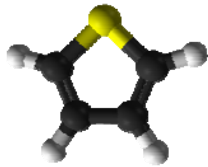
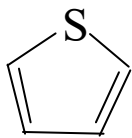
FIG. 1. (a) Molecular structure and (b) and (c) crystalline structure of pentacene. (d) Typical OTFT geometry (top contact), (e) O/OH terminated Silicon oxide, (f) H atom terminated Si.

polymer example:

poly(3-hexylthiophene), P3HT

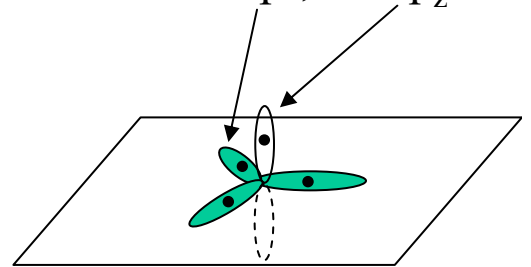


The thiophene ring



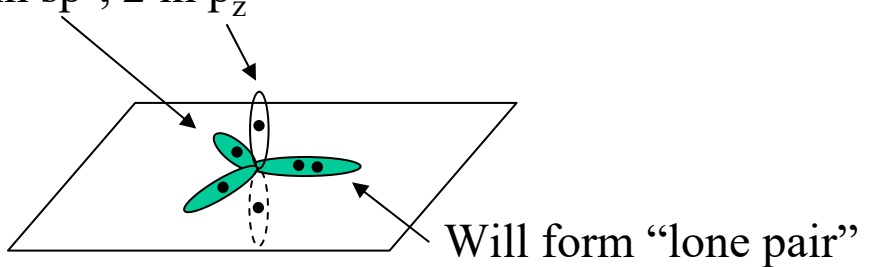
C:  $2s^2 2p^2$

$sp^2$  hybridization: 3 in  $sp^2$ , 1 in  $p_z$

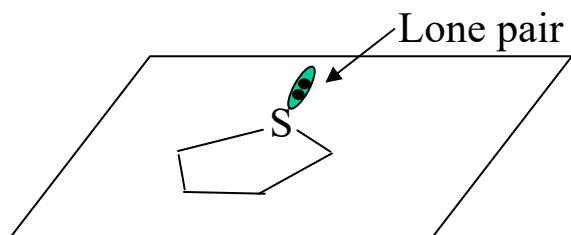


S:  $3s^2 3p^4$

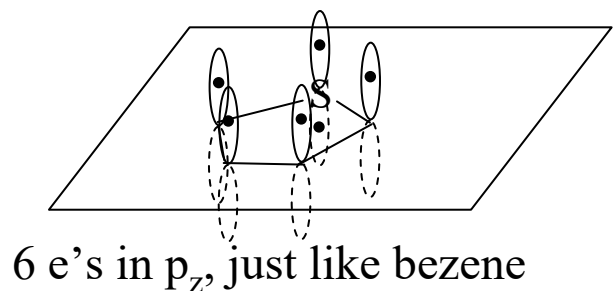
$sp^2$  hybridization: 4 in  $sp^2$ , 2 in  $p_z$



$\sigma$  backbone of thiophene



$p_z$  electron to form  $\pi$  system:



# Two-dimensional charge transport in self-organized, high-mobility conjugated polymers

H. Sirringhaus\*, P. J. Brown\*, R. H. Friend\*, M. M. Nielsen†, K. Bechgaard‡, B. M. W. Langeveld-Voss‡, A. J. H. Spiering‡, R. A. J. Janssen‡, E. W. Meijer‡, P. Herwig§ & D. M. de Leeuw§

\* Cavendish Laboratory, University of Cambridge, Madingley Road, Cambridge CB3 0HE, UK

† Condensed Matter Physics and Chemistry Department, Risø National Laboratory, 4000 Roskilde, Denmark

‡ Laboratory of Macromolecular and Organic Chemistry, Eindhoven University of Technology, 5600 MB Eindhoven, The Netherlands

§ Philips Research Laboratories, Prof. Holstlaan 4, 5656 AA Eindhoven, The Netherlands

Self-organization in many solution-processed, semiconducting conjugated polymers results in complex microstructures, in which ordered microcrystalline domains are embedded in an amorphous matrix<sup>1</sup>. This has important consequences for electrical properties of these materials: charge transport is usually limited by the most difficult hopping processes and is therefore dominated by the disordered matrix, resulting in low charge-carrier mobilities<sup>2</sup> ( $\leq 10^{-5} \text{ cm}^2 \text{ V}^{-1} \text{ s}^{-1}$ ). Here we use thin-film, field-effect transistor structures to probe the transport properties of the ordered microcrystalline domains in the conjugated polymer poly(3-hexylthiophene), P3HT. Self-organization in P3HT results in a lamella structure with two-dimensional conjugated sheets formed by interchain stacking. We find that, depending on processing conditions, the lamellae can adopt two different orientations—parallel and normal to the substrate—the mobilities of which differ by more than a factor of 100, and can reach values as high as  $0.1 \text{ cm}^2 \text{ V}^{-1} \text{ s}^{-1}$  (refs 3, 4). Optical spectroscopy of the field-induced charge, combined with the mobility anisotropy, reveals the two-dimensional interchain character of the polaronic charge carriers, which exhibit lower relaxation energies than the corresponding radical cations on isolated one-dimensional chains. The possibility of achieving high mobilities via two-dimensional transport in self-organized conjugated lamellae is important for applications of polymer transistors in logic circuits<sup>5</sup> and active-matrix displays<sup>4,6</sup>.

We have studied the microstructure of 70–100 nm, spin-coated, regioregular P3HT films by grazing-incidence X-ray diffraction (XRD) on parts of the same SiO<sub>2</sub>/Si substrates on which field-effect transistor (FET) devices were fabricated. Regioregularity denotes the percentage of stereoregular head-to-tail (HT) attachments of the hexyl side chains to the 3-position of the thiophene rings<sup>7</sup>. Two different orientations of the microcrystalline P3HT domains with respect to the FET substrate have been identified (Fig. 1). They are evident from the different intensity distributions of the (100) reflections due to the lamella layer structure and the (010) reflections due to  $\pi$ - $\pi$  interchain stacking<sup>8</sup>. In samples with high regioregularity (>91%) and low molecular weight the preferential orientation of ordered domains is with the (100)-axis normal to the film and the (010)-axis in the plane of the film (Fig. 1a). In contrast, in samples with low regioregularity (81%) and high molecular weight, the crystallites are preferentially oriented with the (100)-axis in the plane and the (010)-axis normal to the film (Fig. 1b)<sup>9</sup>. The cause of this surprising change of orientation is not fully understood. It must be a dynamic phenomenon during the rapid growth of spin-coated films affected by either regioregularity or molecular weight. In films prepared by slow casting from a dilute solution the (100)-axis is normal to the film for all polymers (green trace in Fig. 1c and d).

However, the ability to induce different orientations allows us to establish a direct correlation between the direction of  $\pi$ - $\pi$  stacking and the in-plane FET mobility  $\mu$  (Fig. 2a). At room temperature the highest mobilities of  $0.05$ – $0.1 \text{ cm}^2 \text{ V}^{-1} \text{ s}^{-1}$  are observed for the sample with the highest regioregularity (96%) and the largest size of crystallites with in-plane orientation of the (010)-axis ( $\sim 95 \text{ \AA}$ , as estimated from (010) line shape analysis<sup>10</sup>). For spin-coated samples with HT  $\approx 81\%$ , in which the (010)-axis is normal to the film, the mobility is only  $2 \times 10^{-4} \text{ cm}^2 \text{ V}^{-1} \text{ s}^{-1}$  in spite of pronounced in-plane crystallinity along the (100)-axis with a grain size of  $130 \text{ \AA}$ . No clear correlation between FET mobility and weight average molecular weight  $M_w$  could be established, as seen previously between conductivity and  $M_w$  in highly doped P3HT (ref. 11). This is consistent with the FET mobility being limited by  $\pi$ - $\pi$  interchain rather than intrachain transport as discussed below. In the case of the low-regioregularity polymers it is possible to directly compare mobilities for the in-plane (cast films) and out-of-plane orientation (spin-coated films) of the  $\pi$ - $\pi$  stacking direction (Fig. 1d). In cast films of the 81% polymer the mobility is higher by more than an

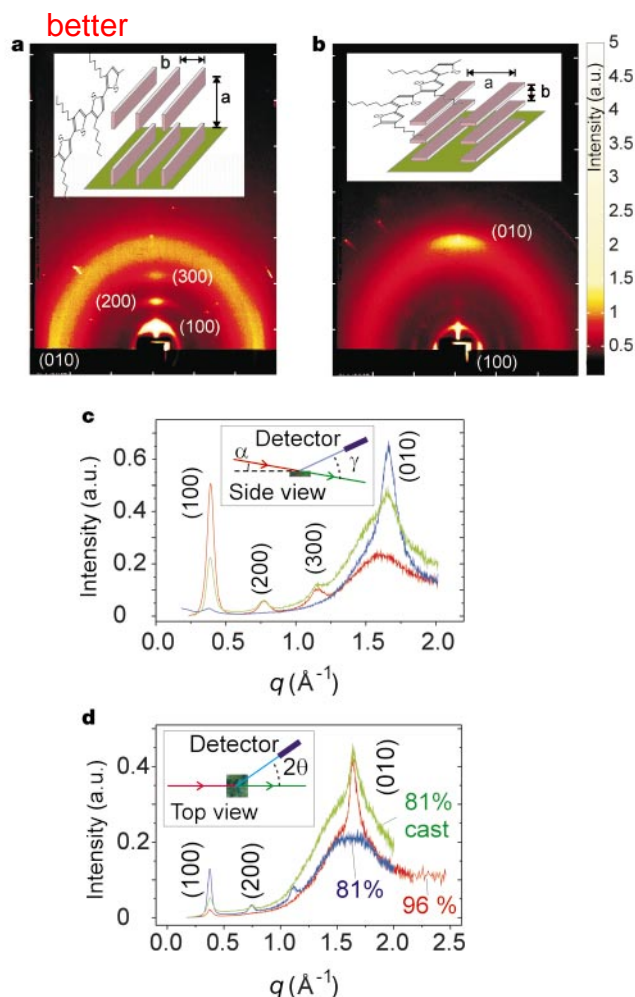


**Figure 1** Two different orientations of ordered P3HT domains with respect to the FET substrate. **a, b**, The wide-angle X-ray scattering images are a colour representation of the two-dimensional distribution of scattered Cu K $\alpha$  X-ray intensity from spin-coated, 70–100 nm thick P3HT films with regioregularity of 96% (**a**) and 81% (**b**) on SiO<sub>2</sub>/Si substrates. The vertical (horizontal) axes correspond to scattering normal (parallel) to the plane of the film. The insets show schematically the different orientations of the microcrystalline grains with respect to the substrate. **c, d**, The change of orientation is confirmed by high-resolution synchrotron X-ray diffraction measurements for constant, grazing-incidence angle with out-of-plane (**c**) and in-plane (**d**) scattering geometry. Red, 96%, spin coated; blue, 81%, spin coated; green, 81%, solution-cast. The intensities plotted versus the total scattering vector are corrected for polarization and geometric factors<sup>10</sup>.

order of magnitude than in spin-coated samples and only slightly lower than that of the highly regioregular polymers (Fig. 2a).

The large mobility anisotropy caused by different preferential orientations of the ordered, microcrystalline domains is clear evidence that the transport is no longer dominated by the remaining amorphous regions of the polymer film but is starting to reflect the transport properties of charge carriers in ordered polymer domains. The highest mobilities of  $0.1 \text{ cm}^2 \text{ V}^{-1} \text{ s}^{-1}$  and the mobility anisotropy for in- and out-of-plane  $\pi$ - $\pi$  stacking of  $\sim 100$  are of the same order of magnitude as in di-hexyl sexithiophene oligomer single crystals<sup>12</sup>. The residual disorder in the films manifests itself in a thermally activated mobility at low temperatures (Fig. 2b). This is interpreted in terms of a distribution of disorder-induced, deeply localized states below the high-mobility electronic states at which charge transport occurs. The activation energies  $E_a$  extracted between room temperature and 150 K ( $\mu \propto \exp(-E_a/kT)$ ) are comparable for the different polymers ( $E_a = 84 \text{ meV}$  (96%),  $100 \text{ meV}$  (95%),  $115 \text{ meV}$  (81%)) suggesting similar degrees of disorder. From our experiments, the intrinsic mobility limit of a hypothetical P3HT single crystal cannot be estimated. However, we have entered a transport regime, in which at room temperature and high gate voltages the Fermi level at the interface is sufficiently close to the charge transport level that intrinsic transport effects such as mobility anisotropies reflecting local polymer self-organization can be observed.

We conclude that the high mobilities of  $0.1 \text{ cm}^2 \text{ V}^{-1} \text{ s}^{-1}$  reported recently<sup>3,4</sup> for the parallel orientation reflect efficient interchain transport in the two-dimensional conjugated lamellae. We discuss how these strong  $\pi$ - $\pi$  interchain interactions may affect the nature of the charge-carrying species. Charge carriers in disordered polymers can be regarded as molecular radical cations formed on isolated, finite conjugated segments of the chain between two conjugation defects<sup>13</sup>. Due to polaronic relaxation of the local electronic and lattice structure the energy levels of a radical cation are shifted relative to those of the neutral molecule, giving rise to additional optical transitions upon charge injection (Fig. 3a). Charge modulation spectroscopy (CMS) measures changes of the optical transmission of a semitransparent FET upon gate-voltage induced modulation of the charge carrier density in the accumulation layer. It yields direct spectroscopic information about the charge carriers in polymer FETs (refs 14, 15) without the disturbing effects of counterions that are present in chemical doping experiments. The CMS spectra clearly show charge-induced, sub-gap transitions giving direct evidence for the polaronic nature of the

charge carriers. For 81% (96%) samples we observe a strong transition at 1.70 eV (1.75 eV), a second transition appearing as a shoulder at  $1.35 \pm 0.05 \text{ eV}$  (Fig. 3a), and a third transition at 0.35 eV (0.32 eV) in the mid-infrared spectral range (Fig. 3b). The associated bleaching—that is, reduction of the strength of the  $\pi$ - $\pi^*$  absorption ( $\Delta T/T > 0$ )—of those chains on which the charges are located (Fig. 3a) exhibits pronounced vibronic structure, which is more structured and red-shifted compared to the inhomogeneously broadened absorption spectrum of the film (P.J.B., H.S. and R.H.F., manuscript in preparation). This shows that the charge carriers observed in CMS have migrated to the most ordered domains in the film; this allows us to claim that the CMS spectra reported here yield the intrinsic spectroscopic signature of charge carriers in ordered P3HT domains. This is further corroborated by the observation that the CMS spectra in the visible and near-infrared exhibit no significant dependence of the relative intensities, energies, or the number of transitions on temperature  $T$  (100–300 K), modulation frequency, and carrier density (P.J.B., H.S. and R.H.F., manuscript in preparation). Therefore, the observed charge-induced transitions must belong to the same physical species, in contrast to CMS studies on oligothiophenes<sup>15</sup> and less-ordered P3HT (ref. 14), in which there is coexistence of singly-charged radical cations, and doubly-charged dications and  $\pi$ -dimers. The observation of just one type of carrier in self-organized P3HT FETs is a manifestation of the low density of chemical and structural defects that may stabilize other carriers. From the independence of the CMS spectra with respect to temperature and charge carrier density we conclude that the carriers are singly-charged. Doubly-charged carriers would tend to dissociate at high temperatures and low carrier densities<sup>16</sup>.

In order to identify the spectroscopic signature of interchain interaction effects we compare the CMS spectra of P3HT FETs with chemical doping experiments on isolated oligo- and polythiophene radical cations ( $nT^+$ ) in solution<sup>16,17</sup>. For  $nT^+$  two characteristic optical transitions, C1 and C2, are observed. Their energy red-shifts monotonically with increasing conjugation length (Fig. 3a). A third transition C3 is symmetry-forbidden on isolated chains<sup>16</sup> and is not observed in the  $nT^+$  spectra. The CMS spectra of self-organized P3HT presented here reveal characteristic features that cannot be understood as an extrapolation of the  $nT^+$  radical cation spectra to long conjugation lengths: (1) We observe three transitions at 0.3–0.35 eV, 1.35 eV and 1.75 eV, the strongest of which (at 1.75 eV) is at significantly higher energy  $E$  than the charge-induced transitions of isolated  $nT^+$ . It blue-shifts towards the  $\pi$ - $\pi^*$  transition with increasing regioregularity ( $\Delta E \approx 50 \text{ meV}$  between 81% and 96%)

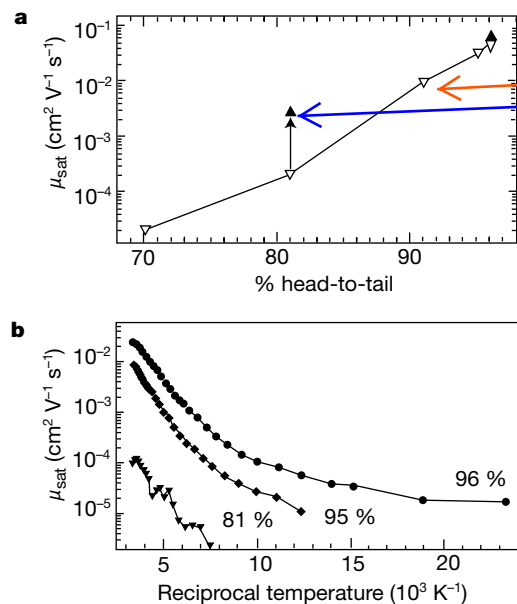


**Figure 2** Charge carrier mobility of P3HT field-effect transistors with different microstructures. **a**, Dependence of the room-temperature mobility on the regioregularity for spin-coated (downward triangles) and solution-cast (upward triangles) top-contact P3HT FETs (channel length  $L = 75 \mu\text{m}$ , channel width  $W = 1.5 \text{ mm}$ ). **b**, Temperature dependence of the field-effect mobility extracted from the characteristics of spin-coated bottom-contact P3HT FETs in the saturation regime ( $L = 10 \mu\text{m}$ ,  $W = 3 \text{ mm}$ ). Measurements were performed in vacuum ( $p < 1 \times 10^{-6} \text{ mbar}$ ) to prevent charge trapping by adsorbed atmospheric impurities. The mobility of top-contact FETs with Au source–drain contacts evaporated after deposition of the polymer is higher, typically by a factor of two, than that of bottom-contact devices<sup>4</sup>.

whereas the infrared transition at  $\sim 0.35$  eV red-shifts. (2) Below  $\sim 0.3$  eV we observe low-energy transitions (CT) extending into the energy range of sharp charge-induced, vibrational ‘amplitude modes’ (AM)<sup>18</sup>. The intensity of the low-energy CT feature increases with regioregularity. Their overlap with the AM results in a sharp dip at 0.18 eV, which may be due to a Fano-type resonance caused by interactions of a discrete level with a continuum<sup>19</sup>. (3) The charge-induced transitions exhibit no vibronic structure in contrast to those of isolated oligomers, while at the same time the associated bleaching signal has a pronounced vibronic structure.

We regard these three characteristic features, not present in isolated radical cation spectra, as an experimental determination of the spectroscopic signature of the two-dimensional nature of charge carriers in the two-dimensional conjugated lamellae of ordered P3HT. In the presence of strong  $\pi$ - $\pi$  interchain interactions, for which the microstructure-mobility correlation gives clear evidence, **the carriers should no longer be confined to a single chain. Although the carriers still have a polaronic nature, requiring their wavefunctions to be localized, they have a pronounced interchain character,** with wavefunctions spreading over neighbouring chains<sup>20,21</sup>. This provides an explanation for the observed shift of

the energy levels towards the highest occupied ( $\pi$ ) and lowest unoccupied ( $\pi^*$ ) molecular orbitals (Fig. 3a), reflecting **a lowering of the polaronic relaxation energy**. The transitions at 0.35 eV, 1.35 eV and 1.75 eV may be related to the C1, C2 and C3 transitions, respectively, of the one-electron model of isolated radical-cations (Fig. 3a, C1 + C2  $\approx$  C3). It has been suggested that, in the presence of interchain interactions, transitions such as C3 (that are symmetry-forbidden in isolated molecules) may become intense<sup>21</sup>. However, for a full theoretical understanding of the spectra a proper treatment of interchain and electron-electron interactions will be required. In the case of small relaxation energies and strong interchain interactions one may expect that due to configuration interactions<sup>16</sup> charge-transfer like transitions (CT in Fig. 3) may become intense. They may explain the intense infrared absorption  $< 0.3$  eV.

The evidence for an association of high-mobility with two-dimensional charge transport provides a firm basis for exploring supramolecular self-organization to enhance charge transport in conjugated polymer semiconductors. By better control of structural anisotropy, and by developing polymers with more strongly  $\pi$ - $\pi$  interacting building blocks<sup>22</sup>, even higher mobilities and, possibly, a truly delocalized transport regime may be reached. □

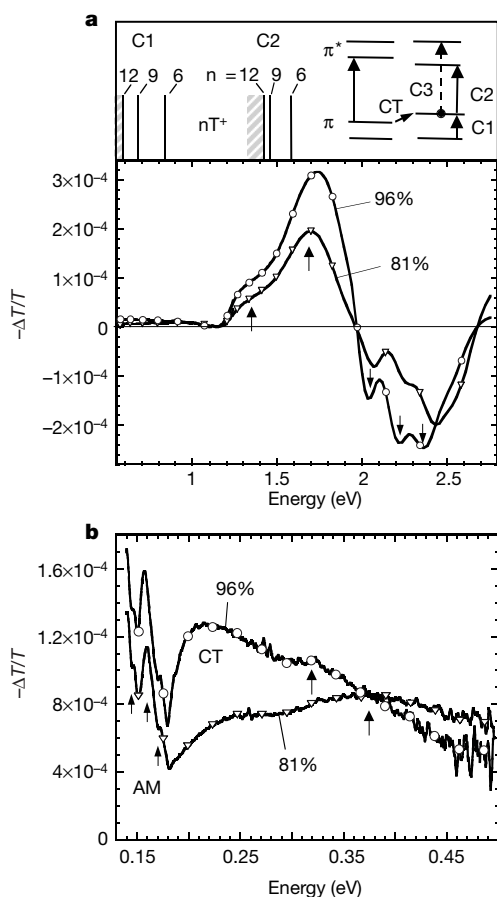


**Figure 3** Charge modulation spectroscopy of semitransparent P3HT FETs in the accumulation regime. The devices were prepared under the same conditions and with similar mobilities as standard FETs and XRD samples (circles—96%, triangles—81%).

**a, b.** The spectra show the **fractional change of the optical transmission upon modulation of the gate voltage** as a function of photon energy in the near-infrared and visible **(a)** and mid-infrared spectral range **(b)** ( $T = 300$  K). Inset: schematic one-electron energy levels of neutral molecules and isolated radical cations, with the experimental energy value of the C1 and C2 transitions of  $nT^+$  oligothiophene radical cations in solution (taken from ref. 16) shifting to lower energies with increasing  $n$ . In the solid state the transitions would be expected to be further red-shifted due to dielectric polarization effects. From the X-ray diffraction correlation lengths the conjugation length of the P3HT polymer is estimated to be  $n \approx 20$ –25.

**Methods**

Samples with HT regioregularity of 70% and 81% (molecular weight  $M_w = 126$  kg mol<sup>-1</sup> and 175 kg mol<sup>-1</sup>, respectively; polydispersity  $D = 2.5$ –2.7) were synthesized by oxidative coupling with FeCl<sub>3</sub>. Following the McCullough route, P3HT with regioregularity of 91% and 95% HT ( $M_w = 11$  and 28 kg mol<sup>-1</sup>,  $D = 1.4$ ) was obtained. The highest regioregularity was a 96% HT sample synthesized by the Rieke route ( $M_w = 28$  kg mol<sup>-1</sup>,  $D = 1.4$ ). For a review of the different synthesis routes see ref. 7. The regioregularity was determined by <sup>1</sup>H-NMR by comparing the signal intensities at 2.80 and 2.60 p.p.m. This yields a lower but more reliable value than analysis of the aromatic region of the spectrum. Films were spin-coated from a 0.8 weight % solution in CHCl<sub>3</sub> onto FET substrates (230 nm SiO<sub>2</sub> gate insulator on top of n<sup>+</sup>-Si gate electrodes) treated with the silylating agent hexamethyldisilazane to promote self-organization.

X-ray diffraction measurements were performed under inert He atmosphere to minimize air scattering and beam damage. A grazing incidence angle below the critical angle of total reflection from the substrate, but above the critical angle for the film, was chosen to enhance the sensitivity to the thin polymer film. Synchrotron XRD measurements were performed at the BW2 beamline of the German electron synchrotron facility (DESY) in Hamburg.

Received 12 March; accepted 3 August 1999.

- Samuelsen, E. J. & Mårdalen, J. in *Handbook of Organic Conductive Molecules and Polymers* Vol. 3 (eds Nalwa, H. S.) 87–120 (Wiley, Chichester, UK, 1997).
- Kobashi, M. & Takeuchi, H. Inhomogeneity of spin-coated and cast non-regioregular poly(3-hexylthiophene) films. Structures and electrical and photophysical properties. *Macromolecules* **31**, 7273–7278 (1998).
- Bao, Z., Dodabalapur, A. & Lovinger, A. J. Soluble and processable regioregular poly(3-hexylthiophene) for thin film field-effect transistor applications with high mobility. *Appl. Phys. Lett.* **69**, 4108–4110 (1996).
- Sirringhaus, H., Tessler, N. & Friend, R. H. Integrated optoelectronic devices based on conjugated polymers. *Science* **280**, 1741–1744 (1998).
- Drury, C. J., Mutsaers, C. M. J., Hart, C. M., Matters, M. & deLeeuw, D. M. Low-cost all-polymer integrated circuits. *Appl. Phys. Lett.* **73**, 108–110 (1998).
- Dodabalapur, A. et al. Organic smart pixels. *Appl. Phys. Lett.* **73**, 142–144 (1998).
- McCullough, R. D. The chemistry of conducting polythiophenes. *Adv. Mater.* **10**, 93–116 (1998).
- Prosa, T. J., Winokur, M. J., Moulton, J., Smith, P. & Heeger, A. J. X-ray structural studies of poly(3-alkylthiophenes)—An example of an inverse comb. *Macromolecules* **25**, 4364–4372 (1992).
- Fell, H. J., Samuelsen, E. J., Als-Nielsen, J., Grübel, G. & Mårdalen, J. Unexpected orientational effects in spin-cast, sub-micron layers of poly(alkylthiophene): A diffraction study with synchrotron radiation. *Solid State Commun.* **94**, 843–846 (1995).
- Warren, B. E. *X-ray Diffraction* 41–50 (Addison-Wesley, Reading, USA, 1969).
- Ishikawa, H. et al. Effect of molecular mass of poly(3-alkylthiophene) on electrical properties. *J. Phys. D* **25**, 897–900 (1992).
- Schön, J. H., Kloc, C., Laudise, R. A. & Batlogg, B. Electrical properties of single crystals of rigid rodlike conjugated molecules. *Phys. Rev. B* **58**, 12952–12957 (1998).
- Deussen, M. & Bässler, H. Anion and cation absorption spectra of conjugated oligomers and polymer. *Synth. Met.* **54**, 49–55 (1993).
- Ziemelis, K. E. et al. Optical spectroscopy of field-induced charge in poly(3-hexyl thiophene) metal-insulator-semiconductor structures: Evidence for polarons. *Phys. Rev. Lett.* **66**, 2231–2234 (1991).
- Harrison, M. G., Fichou, D., Garnier, F. & Yassar, A. *In situ* charge-modulation spectroscopy of oligothiophene field-effect diodes: from sexithiophene towards polythiophene. *Opt. Mater.* **9**, 53–58 (1998).
- Haare, J. A. E. H. V. et al. Redox states of long oligothiophenes: Two polarons on a single chain. *Chem. Eur. J.* **4**, 1509–1522 (1998).
- Horowitz, G., Yassar, A. & Bardeleben, H. J. V. ESR and optical spectroscopy evidence for a chain

- length dependence of the charged states of thiophene oligomers. Extrapolation to polythiophene. *Synth. Met.* **62**, 245–252 (1994).
18. Horowitz, B. Infrared activity of Peierls systems and application to polyacetylene. *Solid State Commun.* **41**, 729–734 (1982).
  19. Fano, U. Effects of configuration interaction on intensities and phase shifts. *Phys. Rev.* **124**, 1866–1878 (1961).
  20. Emin, D. Self-trapping in quasi-one-dimensional solids. *Phys. Rev. B* **33**, 3973–3975 (1986).
  21. Blackman, J. A. & Sabra, M. K. Interchain coupling and optical absorption in degenerate and nondegenerate polymers. *Phys. Rev. B* **47**, 15437–15448 (1993).
  22. Sirringhaus, H. *et al.* Bis(dithienothiophene) organic field-effect transistors with a high ON/OFF ratio. *Appl. Phys. Lett.* **71**, 3871–3873 (1997).

## Acknowledgements

We thank J. Cornil, D. Dos Santos, and A. J. Flewitt for contributions. Financial support from the European Commission and the Training and Mobility of Researchers (TMR) programme is acknowledged. H.S. thanks the Royal Society for a University Research Fellowship.

Correspondence and requests for materials should be addressed to H.S. (e-mail: hs220@phy.cam.ac.uk).

## Identifying magma–water interaction from the surface features of ash particles

Ralf Büttner\*, Pierfrancesco Dellino† & Bernd Zimanowski\*

\* *Physikalisch Vulkanologisches Labor, Institut für Geologie, Universität Würzburg, Pleicherwall 1, D-97070 Würzburg, Germany*

† *Dipartimento Geomineralogico, Università degli Studi di Bari, Via Orabona 4, I-70125 Bari, Italy*

The deposits from explosive volcanic eruptions (those eruptions that release mechanical energy over a short time span<sup>1</sup>) are characterized by an abundance of volcanic ash<sup>2,3</sup>. This ash is produced by fragmentation of the magma driving the eruption and by fragmenting and ejecting parts of the pre-existing crust (host rocks). Interactions between rising magma and the hydrosphere (oceans, lakes, and ground water) play an important role in explosive volcanism<sup>4,5</sup>, because of the unique thermodynamic

properties of water that allow it to very effectively convert thermal into mechanical energy. Although the relative proportion of magma to host-rock fragments is well preserved in the pyroclastic rocks deposited by such eruptions, it has remained difficult to quantitatively assess the interaction of magma with liquid water from the analysis of pyroclastic deposits<sup>2–5</sup>. Here we report the results of a study of natural pyroclastic sequences combined with scaled laboratory experiments. We find that surface features of ash grains can be used to identify the dynamic contact of magma with liquid water. The abundance of such ash grains can then be related to the water/magma mass ratios during their interaction.

From direct observation of ‘wet’ volcanic eruptions (phreatomagmatic eruptions) and the analysis of their deposits, several criteria have been defined that qualitatively indicate the presence of liquid water during an eruption<sup>2,3,6,7</sup>. The reconstruction of volcanic eruptions from their deposits, however, would benefit from a tool that could quantitatively indicate the amount of liquid water that encountered the magma. A perfect laboratory volcano for investigations of magma–water contact is the active Italian volcanic island of Vulcano and its young crater, La Fossa, where various kinds of phreatomagmatic deposits, spanning the range of water–magma phenomenologies reported in the literature, are present.

Phreatomagmatic deposits at La Fossa di Vulcano have formed during almost all of the numerous eruptions characterizing its volcanic history, which started ~6,000 years ago, with the last eruption being the ‘vulcanian’ one of AD 1888–1890 (ref. 8). Following the scheme used in the literature<sup>9–11</sup>, these deposits have been subdivided into two categories: ‘wet’ and ‘dry’ surge deposits, both being the products of laterally moving surges of low-density ash clouds. The difference between the two types is evidenced by their structural and textural features. ‘Dry’-type deposits are decimetres to metres thick densely laminated layers of coarse ash and lapilli; ‘wet’-type deposits are mostly not internally structured (that is, “massive”) centimetres thick fine-ash layers with features such as accretionary lapilli, vesiculated tuff, and plastic type deformation<sup>7</sup>.

Various structures of deposits have been interpreted using results from early magma–water interaction experiments<sup>12</sup>. In ‘dry’ explosions the interaction is suggested to be more effective, with all water consumed during interaction and transformed into superheated steam, whereas in ‘wet’ explosions, the interaction is less effective,

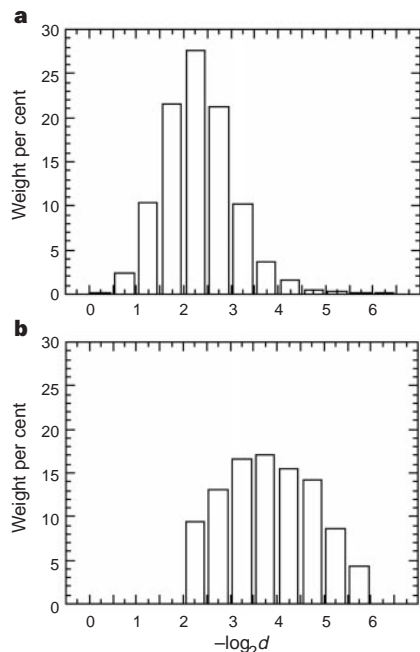


**Figure 1** Grain size distribution of phreatomagmatic deposits of La Fossa di Vulcano. The figures show the proportional importance of grain size fractions in weight per cent ( $d$  is the sieve mesh size in millimetres). **a**, Histogram of a representative ‘dry’ surge deposit. **b**, Histogram of a representative ‘wet’ surge deposit.

## Two-dimensional charge transport in self-organized, high-mobility conjugated polymers

H. Sirringhaus<sup>\*</sup>, P. J. Brown<sup>\*</sup>, R. H. Friend<sup>\*</sup>, M. M. Nielsen<sup>†</sup>, K. Bechgaard<sup>‡</sup>, B. M. W. Langeveld-Voss<sup>‡</sup>, A. J. H. Spiering<sup>‡</sup>, R. A. J. Janssen<sup>‡</sup>, E. W. Meijer<sup>‡</sup>, P. Herwig<sup>§</sup> & D. M. de Leeuw<sup>§</sup>

<sup>\*</sup> Cavendish Laboratory, University of Cambridge, Madingley Road, Cambridge CB3 0HE, UK

<sup>†</sup> Condensed Matter Physics and Chemistry Department, Risø National Laboratory, 4000 Roskilde, Denmark

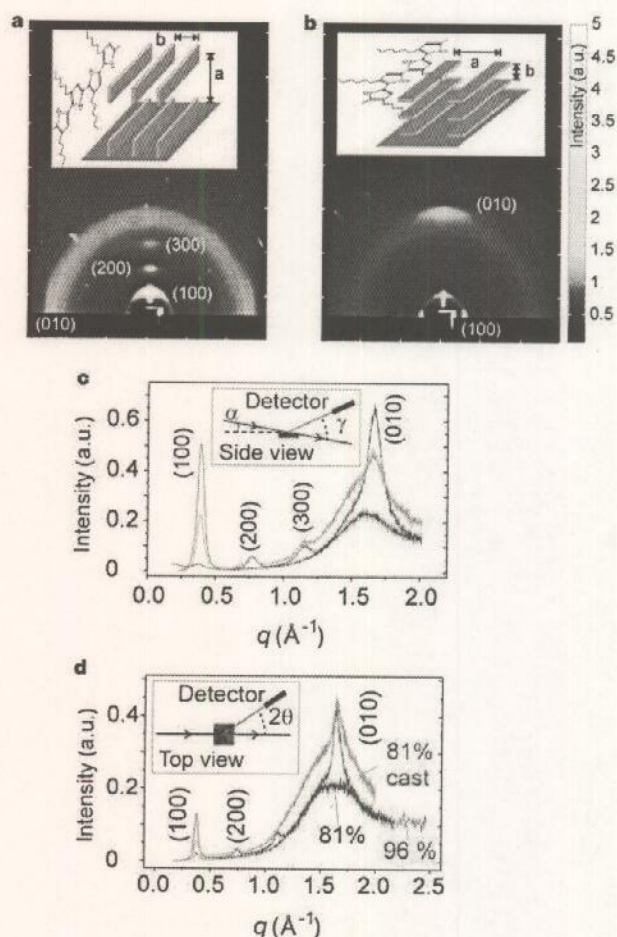
<sup>‡</sup> Laboratory of Macromolecular and Organic Chemistry, Eindhoven University of Technology, 5600 MB Eindhoven, The Netherlands

<sup>§</sup> Philips Research Laboratories, Prof. Holstlaan 4, 5656 AA Eindhoven, The Netherlands

Self-organization in many solution-processed, semiconducting conjugated polymers results in complex microstructures, in which ordered microcrystalline domains are embedded in an amorphous matrix<sup>1</sup>. This has important consequences for electrical properties of these materials: charge transport is usually limited by the most difficult hopping processes and is therefore dominated by the disordered matrix, resulting in low charge-carrier mobilities<sup>2</sup> ( $\leq 10^{-5}$  cm<sup>2</sup> V<sup>-1</sup> s<sup>-1</sup>). Here we use thin-film, field-effect transistor structures to probe the transport properties of the ordered microcrystalline domains in the conjugated polymer poly(3-hexylthiophene), P3HT. Self-organization in P3HT results in a lamella structure with two-dimensional conjugated sheets formed by interchain stacking. We find that, depending on processing conditions, the lamellae can adopt two different orientations—parallel and normal to the substrate—the mobilities of which differ by more than a factor of 100, and can reach values as high as 0.1 cm<sup>2</sup> V<sup>-1</sup> s<sup>-1</sup> (refs 3, 4). Optical spectroscopy of the field-induced charge, combined with the mobility anisotropy, reveals the two-dimensional interchain character of the polaronic charge carriers, which exhibit lower relaxation energies than the corresponding radical cations on isolated one-dimensional chains. The possibility of achieving high mobilities via two-dimensional transport in self-organized conjugated lamellae is important for applications of polymer transistors in logic circuits<sup>5</sup> and active-matrix displays<sup>4,6</sup>.

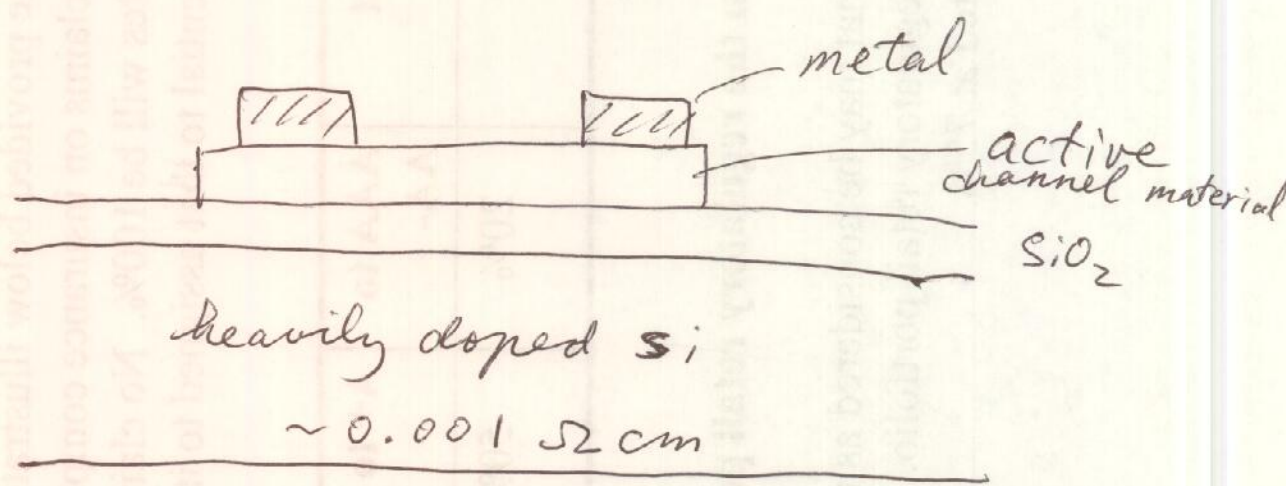
We have studied the microstructure of 70–100 nm, spin-coated, regioregular P3HT films by grazing-incidence X-ray diffraction (XRD) on parts of the same SiO<sub>2</sub>/Si substrates on which field-effect transistor (FET) devices were fabricated. Regioregularity denotes the percentage of stereoregular head-to-tail (HT) attachments of the hexyl side chains to the 3-position of the thiophene rings<sup>7</sup>. Two different orientations of the microcrystalline P3HT domains with respect to the FET substrate have been identified (Fig. 1). They are evident from the different intensity distributions of the (100) reflections due to the lamella layer structure and the (010) reflections due to  $\pi$ - $\pi$  interchain stacking<sup>8</sup>. In samples with high regioregularity (>91%) and low molecular weight the preferential orientation of ordered domains is with the (100)-axis normal to the film and the (010)-axis in the plane of the film (Fig. 1a). In contrast, in samples with low regioregularity (81%) and high molecular weight, the crystallites are preferentially oriented with the (100)-axis in the plane and the (010)-axis normal to the film (Fig. 1b)<sup>9</sup>. The cause of this surprising change of orientation is not fully understood. It must be a dynamic phenomenon during the rapid growth of spin-coated films affected by either regioregularity or molecular weight. In films prepared by slow casting from a dilute solution the (100)-axis is normal to the film for all polymers (green trace in Fig. 1c and d).

However, the ability to induce different orientations allows us to establish a direct correlation between the direction of  $\pi$ - $\pi$  stacking and the in-plane FET mobility  $\mu$  (Fig. 2a). At room temperature the highest mobilities of 0.05–0.1 cm<sup>2</sup> V<sup>-1</sup> s<sup>-1</sup> are observed for the sample with the highest regioregularity (96%) and the largest size of crystallites with in-plane orientation of the (010)-axis ( $\sim 95$  Å, as estimated from (010) line shape analysis<sup>10</sup>). For spin-coated samples with HT  $\approx 81\%$ , in which the (010)-axis is normal to the film, the mobility is only  $2 \times 10^{-4}$  cm<sup>2</sup> V<sup>-1</sup> s<sup>-1</sup> in spite of pronounced in-plane crystallinity along the (100)-axis with a grain size of 130 Å. No clear correlation between FET mobility and weight average molecular weight  $M_w$  could be established, as seen previously between conductivity and  $M_w$  in highly doped P3HT (ref. 11). This is consistent with the FET mobility being limited by  $\pi$ - $\pi$  interchain rather than intrachain transport as discussed below. In the case of the low-regioregularity polymers it is possible to directly compare mobilities for the in-plane (cast films) and out-of-plane orientation (spin-coated films) of the  $\pi$ - $\pi$  stacking direction (Fig. 1d). In cast films of the 81% polymer the mobility is higher by more than an



**Figure 1** Two different orientations of ordered P3HT domains with respect to the FET substrate. **a, b**, The wide-angle X-ray scattering images are a colour representation of the two-dimensional distribution of scattered Cu K $\alpha$  X-ray intensity from spin-coated, 70–100 nm thick P3HT films with regioregularity of 96% (**a**) and 81% (**b**) on SiO<sub>2</sub>/Si substrates. The vertical (horizontal) axes correspond to scattering normal (parallel) to the plane of the film. The insets show schematically the different orientations of the microcrystalline grains with respect to the substrate. **c, d**, The change of orientation is confirmed by high-resolution synchrotron X-ray diffraction measurements for constant, grazing-incidence angle with out-of-plane (**c**) and in-plane (**d**) scattering geometry. Red, 96%, spin coated; blue, 81%, spin coated; green, 81%, solution-cast. The intensities plotted versus the total scattering vector are corrected for polarization and geometric factors<sup>10</sup>.

A quick, dirty lazy way to make a transistor or not so dirty!



What happens if the Si substrate is not sufficiently degenerately doped?